

Multiscale modelling framework for the fracture of thin polycrystalline films - Application to polysilicon

Shantanu S. Mulay¹, Gauthier Becker², Renaud Vayrette³, Jean-Pierre Raskin³,
Thomas Pardoën³, Montserrat Galceran^{4,5}, Stéphane Godet⁴, Ludovic Noels^{1,*}
1, University of Liege, Department of Aerospace and Mechanical Engineering,
Computational and Multiscale Mechanics of Materials, Chemin des Chevreuils 1,
B-4000 Liège, Belgium.

2, Massachusetts Institute of Technology, Department of Aeronautics and Astronautics,
77, Massachusetts Avenue, Cambridge, MA 02139-4307, United States

3, Université catholique de Louvain, Institute of Mechanics, Materials and Civil
Engineering, Place Sainte Barbe 2, 1348 Louvain-la-Neuve, Belgium.

4, Université Libre de Bruxelles, Materials Engineering,
characterization, synthesis and recycling, 50 Av. FD Roosevelt CP194/03,
1050 Brussels, Belgium.

5, CIC Energigune, Albert Einstein 48, 01510 Miñano (Álava), Spain

*, Corresponding author: L.Noels@ulg.ac.be, Tel:+32 43669503

Abstract

The Micro-electro-mechanical systems (MEMS) are now widely used in several engineering fields. The control of the deposition process of polycrystalline silicon makes it a key element in the manufacturing of MEMS. The fracture properties of the polycrystalline silicon directly affect the reliability of MEMS in service. Out of the several factors, an effect of the orientation of grains on the fracture behaviour of the polycrystalline silicon films is investigated in the present work. This is achieved firstly, by identifying the statistical variation of the fracture strength and critical strain energy release rate, at nanoscopic scale, over a thin polycrystalline silicon film, having mesoscopic scale dimensions, with the random orientation of grains. Secondly, the thin polycrystalline silicon film is considered at the continuum macroscopic MEMS scale, and its fracture behaviour is studied by incorporating the nanoscopic scale effect of grain orientation. The entire modelling and simulation of the thin polycrystalline silicon film is achieved by combining the discontinuous Galerkin method and extrinsic cohesive law to describe the fracture process. At the end, the fracture stress and strain, at the mesoscopic and macroscopic levels, are found to be closely matching with the corresponding experimental results.

1 Introduction

Polycrystalline silicon (polySi) is the most common material in use for the manufacturing of MEMS. Several factors, such as the grain size, grain orientation, and nano scale defects or flaws, affect the mechanical properties of thin polySi film, such as the Young's modulus E , fracture strength σ_c , and critical strain energy release rate G_c [1]. Apart from this, a specific manufacturing process adopted to produce MEMS also further affect the run-time fracture behaviour of MEMS. It is pertinent at first to clearly define the relevant length scales to illustrate the problem addressed in the present work. The length dimension from 1 nm to 100 nm is referred as the nanoscopic scale, from 100 nm (0.1 μm) to 1000 nm (1.0 μm) is referred as the mesoscopic or microscopic scale, and higher than 1.0 μm is referred as the MEMS or macroscopic scale. Thus, an average single grain size of polySi (≈ 100 nm) falls under the nanoscopic scale, the size of the simulation model of a thin polySi film consisting of several grains fall under the mesoscopic or microscopic scale (size of representative volume element), and finally the size of the simulation model of a thin polySi film having continuum structure, i.e., without the underlying microstructure, falls under the macroscopic length scale. The length scales will be correspondingly referred in the subsequent sections of this paper.

Several advanced techniques [2, 3] have been developed over the years to correctly measure the mechanical properties E , σ_c , and G_c of a bulk polySi and single crystal silicon presenting a preferred out of plane orientation, such as $\langle 1\ 0\ 0 \rangle$ or $\langle 1\ 1\ 0 \rangle$ or $\langle 1\ 1\ 1 \rangle$, involving the statistical aspects, using the micromechanical test structures. These researches report some variations in the mean values of E and σ_c at both, the micro and macroscopic levels. This could be explained by the random orientation of grains at the mesoscopic level leading to a statistical strength distribution at macroscopic level, and thus two samples may have completely different crack paths (transgranular or intergranular) as well as different fracture strengths. The literature also reports a decrease of a fracture strength with respect to an increase in the thickness of the test sample [4]. This could be explained by the presence of more surface flaws across the thickness in the thicker specimen. Thus, all these reasons warrant a robust design procedure of MEMS, made up of polySi, linking the probabilistic nature of the fracture behaviour of polySi at mesoscopic level with the macroscopic level.

The fracture of a thin polySi film involves the nanoscopic scale corresponding to the grain size, as well as the macroscopic scale corresponding to the specimen dimensions. The fracture properties (σ_c , G_c and crack path) of polySi vary at nanoscopic scale due to the several factors mentioned earlier. Therefore, the prediction of the fracture behaviour at MEMS scale is a particularly challenging task that is accomplished through a representative volume element (RVE) with the mesoscopic scale dimensions. The main objective of the present work is to link the effect of the grains orientation at mesoscopic level to the fracture of MEMS at macroscopic level to contribute to more robust design tools. Toward this end, a plane-stress 2-D thin polySi film is modeled at the mesoscopic and macroscopic levels by the discontinuous Galerkin (DG) method coupled with the extrinsic cohesive law (ECL) approach accounting for the fracture process. The DG method takes into account the discontinuities (jump) in the field variable distribution in the interior of the problem domain, and the ECL approach performs the unloading of the force on the newly created fracture surfaces. The values of σ_c and G_c are experimentally available for a single crystal silicon with preferred out of plane grain orientations $\langle 1\ 0\ 0 \rangle$, $\langle 1\ 1\ 0 \rangle$ and $\langle 1\ 1\ 1 \rangle$, despite of a mesoscopic crack experimentally propagates along the weakest plane having a certain "average" orientation (direction) that can be extrapolated by these three orientations. A new formulation

is thus proposed that computes the effective values of σ_c and G_c for an "average" out of plane orientation of the grain by the known three values. Several grains are experimentally observed over the thickness of a thin polySi film [3, 5–7], so it is not exactly a plane stress problem. Here we want to get the fracture along the weakest plane, and not in the normal direction of the loading cross-section. Thus, the thickness of a thin polySi film is considered while identifying the weakest fracture plane for the through-the-thickness fracture.

One of the primary motivations behind this study is that the finite element size of the discretized microstructure is constrained by the smallest grain size present in the model. Indeed, a large number of elements, varying in size, are generated even for a fewer number of grains in a model of the thin polySi film. Therefore, very small load increments are required in order to achieve a stable quasi-static simulation. In fact, an average grain size of approximately 100 nm leads to a time step around $\approx 1 \times e^{-15}$ sec., resulting in a huge computational time even after the parallel implementation of the code. This problem is successfully addressed by the 2-scale method proposed in this work, as one can have a much larger finite element size at the macroscopic length.

The weak form of the DG method is developed similar to the classical finite element method (FEM), except that the boundary integral terms do not vanish. The integration by parts is restricted to the subdomains, thus the boundary integral terms arising from it across the subdomain boundaries are retained and used to capture the discontinuities across the element interfaces. Thus, the unknown field is assumed to be continuous only within the element, and discontinuous across the inter-element boundaries. The theoretical aspects of the DG method are well explained in the available literature [8–11].

The ECL method is one of the types of cohesive zone models (CZM) in which a cohesive zone (process zone) is considered ahead of the crack tip, such that the force on the crack lips within the cohesive zone progressively vanishes, leading to fully open crack. This model was initially proposed by Dugdale [12] (for elastic perfectly plastic material) and extended by Barenblatt [13] for a general elasto-plastic material. The opening of a crack with in CZM is constrained by the traction forces in-between the fracture surfaces. Thus, a monotonically decreasing traction separation law (TSL) results in zero traction values in-between the crack surfaces once the effective crack opening reaches a critical value. The total energy released per unit of the newly created crack surface area (J/m^2) during the crack opening is equal to the fracture energy or critical strain energy release rate G_c . The value of G_c for very brittle materials is almost always equal to 2γ , where γ is the surface energy of the material. The factor 2 is used as two new surfaces are formed during the fracture process. The cohesive laws can be typically implemented in two ways, viz., intrinsic [14] and extrinsic cohesive laws [15, 16]. Historically intrinsic laws have been preferred to extrinsic one as they are easier to implement. Nevertheless the recourse to an intrinsic cohesive law leads to an inconsistent pure penalty method. On the contrary, extrinsic cohesive laws preserve the consistency but they are more complicated to implement in the case of continuous Galerkin methods as some topological mesh modifications are required during the simulation. This issue no longer exists for DG methods as the interface elements are already discontinuous before the insertion of the cohesive element, as in the intrinsic approach [17]. An interface term, ensuring the consistency of the method, is considered in the DG/ECL framework instead of a pure penalty method. As long as the ECL is monotonically decreasing, the shape of the curve does not affect the solution for brittle materials. The detailed discussion and formulation of DG/ECL methods can be found in the references [10, 11].

Firstly, the fracture of polySi thin films is simulated at the mesoscopic level by meshing explicitly several grains present in the RVE. Several sets of the simulation results are obtained, by assigning each time, a random orientation to the grains. A macroscopic cohesive law is then extracted for each set of results [18,19], and the mean and standard deviation values of σ_c and maximum crack tip opening displacement are computed. An average macroscopic cohesive law is then developed based on these values. Secondly, the fracture of a polySi thin film is performed at the macroscopic level, by the average cohesive law, for a much larger model without the underlying microstructure. At both length scales, the fracture is modelled by DG / ECL combination. Finally, all the simulation results (fracture strength and strain) are compared with corresponding experiments.

This paper is organized as follows. The brief formulations of both DG and ECL methods are given in Section 2. The formulations to compute the effective σ_c for a general out-of-plane orientation of grains, and the effect of the thickness of polySi thin film on the effective σ_c for the through-the-thickness crack are included in Section 3. The fracture studies of a thin polySi film is performed, as explained earlier, and their results at the microscopic and macroscopic levels are discussed in Sections 3 and 4, respectively. The simulation results are then compared with the experimental work in Section 5, and finally the conclusions are drawn in Section 6.

2 Discontinuous Galerkin method and extrinsic cohesive law framework

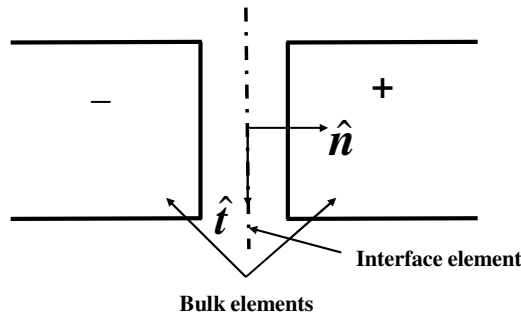


Figure 1: Interface element with local basis vectors in-between the two 2D bulk elements, "-" and "+", in the DG method

The thin polySi film, at the mesoscopic and macroscopic levels, is first treated as a continuum, with a discretization of the grains following the DG method and assuming small deformations. The mesh of the geometry contain bulk elements and all the boundaries between them are treated as interface elements, as shown in Figure 1.

Let $\Omega \subset \mathbf{R}^2$ be a body subjected to a force per unit mass \mathbf{b} (N/Kg). Its boundary surface Γ includes two parts: the Dirichlet boundary denoted by Γ_D , where the displacement \mathbf{u} is prescribed by $\bar{\mathbf{u}}$, and the Neumann boundary denoted by Γ_T , where the traction is prescribed by $\bar{\mathbf{t}}$. One always has $\Gamma = \Gamma_D \cup \Gamma_T$ and $\Gamma_D \cap \Gamma_T = \emptyset$. The

continuum mechanical equilibrium equations in the material form are stated as

$$\nabla \cdot \boldsymbol{\sigma}^T + \rho \mathbf{b} = \rho \ddot{\mathbf{u}} \quad \text{in } \Omega, \quad (1)$$

$$\mathbf{u} = \bar{\mathbf{u}} \quad \text{on } \Gamma_D, \text{ and} \quad (2)$$

$$\boldsymbol{\sigma} \hat{\mathbf{n}} = \bar{\mathbf{t}} \quad \text{on } \Gamma_T. \quad (3)$$

where ρ is the density, $\boldsymbol{\sigma}$ is the Cauchy stress tensor, and $\hat{\mathbf{n}}$ is the outward normal to the unit surface in the current configuration. The situation of cracked interfaces will be considered in the next subsection.

The 2D finite element discretization of the body Ω is expressed as $\Omega = \bigcup_e \bar{\Omega}^e$, where $\bar{\Omega}^e$ is the union of the open domain Ω^e with its boundary Γ^e . Here the symbol Ω is used to represent the whole body and its discretization for simplicity. The weak form of Equations (1-3) arises by seeking a polynomial approximation \mathbf{u} of the displacement field over the discretization Ω . Contrarily to a continuous Galerkin approximation, which requires $\mathbf{u} \in C^0(\Omega)$, the DG approach requires only an element-wise continuous polynomial approximation, *i.e.*, $\mathbf{u} \in C^0(\Omega^e)$. Consequently, for a DG formulation the trial functions \mathbf{w}_u are also discontinuous across the element interfaces on the internal boundary of the body $\Gamma_I = [\bigcup_e \Gamma^e] \setminus \Gamma$.

The new weak formulation of the problem is obtained in a similar way as for the continuous Galerkin approximation. The linear momentum balance is enforced in a weighted average sense by multiplying the strong form (1) by a suitable test function \mathbf{w}_u and by integrating by parts in the domain. However, since both test and trial functions are discontinuous, the integration by parts is not performed over the whole domain but on each element instead. Using traditional DG considerations, see [8] for details, this leads to

$$\begin{aligned} \int_{\Omega} (\rho \ddot{\mathbf{u}} \cdot \mathbf{w}_u + \boldsymbol{\sigma} : \nabla \mathbf{w}_u) dv + \int_{\Gamma_I} [[\mathbf{w}_u]] \cdot \langle \boldsymbol{\sigma} \rangle \cdot \hat{\mathbf{n}}^- ds \\ = \int_{\Omega} \rho \mathbf{b} \cdot \mathbf{w}_u dv + \int_{\Gamma_T} \mathbf{w}_u \cdot \bar{\mathbf{t}} ds \end{aligned} \quad (4)$$

where $\hat{\mathbf{n}}^-$ is the outward normal to the unit surface of the “minus” element on one side of the interface. In this equation, the discretized Cauchy stress tensor $\boldsymbol{\sigma}$ results from the strain tensor $\boldsymbol{\varepsilon} = (1/2)(\nabla \otimes \mathbf{u} + \mathbf{u} \otimes \nabla)$ through a constitutive material law. As the grains of polySi are orthotropic in nature, anisotropic material tensor expressed in the 2D plane-stress state is used such that $\boldsymbol{\sigma} = \mathbf{C} : \boldsymbol{\varepsilon}$. The Equation (4) contains all the usual terms from the classical Galerkin method with an extra terms accounting for the discontinuities of the field at inter element boundaries. We have considered the jump and average operators in these equations, which are defined on an interface of two bulk elements of the discretized geometry, arbitrarily denoted “plus” and “minus” as shown in Figure 1, respectively, as

$$[[\bullet]] = [\bullet^+ - \bullet^-] \quad \text{and} \quad \langle \bullet \rangle = \frac{1}{2} [\bullet^+ + \bullet^-] \quad (5)$$

In the formulation (4) so far, neither the displacement continuity in-between the elements, nor the stability of the method are enforced. The compatibility equation $\mathbf{u}^- - \mathbf{u}^+ = 0$ on Γ_I is enforced through a so-called symmetrization term in $[[\mathbf{u}]]$ and a (sufficiently large) quadratic stabilization term in $[[\mathbf{u}]]$ and $[[\mathbf{w}_u]]$. With the addition of the quadratic terms, the general displacement jumps are stabilized in the numerical solution, while the symmetrization term leads to an optimal convergence rate with

respect to the mesh size. The small deformation material response is thus properly considered for the final weak formulation of the problem, which consists of finding \mathbf{u} such that

$$\left. \begin{aligned} & \int_{\Omega} (\rho \ddot{\mathbf{u}} \cdot \mathbf{w}_u + \boldsymbol{\sigma} : \nabla \mathbf{w}_u) dv + \int_{\Gamma_1} [[\mathbf{w}_u]] \cdot \langle \boldsymbol{\sigma} \rangle \cdot \hat{\mathbf{n}}^- ds + \\ & \int_{\Gamma_1} \left\{ [[\mathbf{w}_u]] \otimes \hat{\mathbf{n}}^- : \left\langle \frac{\beta_s}{h_s} \mathbf{C} \right\rangle : [[\mathbf{u}]] \otimes \hat{\mathbf{n}}^- \right\} ds + \\ & \int_{\Gamma_1} \left\{ [[\mathbf{u}]] \cdot \langle \mathbf{C} : \nabla \mathbf{w}_u \rangle \cdot \hat{\mathbf{n}}^- \right\} ds = \\ & \int_{\Omega} \rho \mathbf{b} \cdot \mathbf{w}_u dv + \int_{\Gamma_T} \mathbf{w}_u \cdot \bar{\mathbf{t}} ds, \quad \forall \mathbf{w}_u \end{aligned} \right\} \quad (6)$$

where h_s and β_s are the mesh size and penalty parameter for stabilization, respectively. The second, third, and fourth terms from Equation (6) are the consistency, stabilization, and compatibility terms, respectively. This formulation, known as the consistent interior penalty method, has been shown stable for β_s larger than a constant that depends on the polynomial approximation. More details and specific derivations about the DG formulation can be found in [8–11].

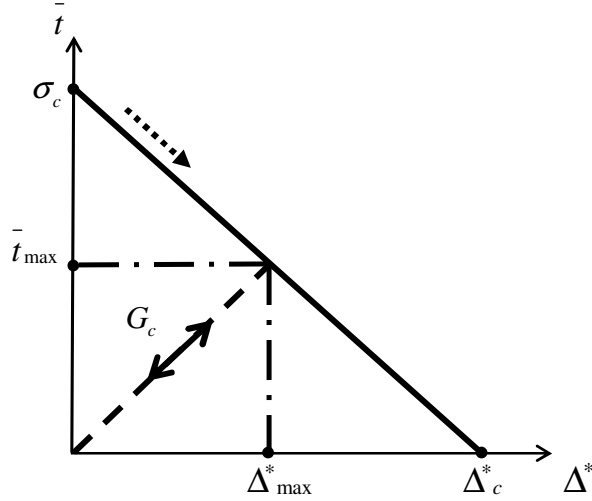


Figure 2: Linearly decreasing extrinsic cohesive law

Linearly decreasing ECL, as shown in Figure 2, is considered in the present work to model the crack opening in-between the two fracture surfaces. Here σ_c , G_c , Δ^* and Δ_{\max}^* are the fracture strength, critical strain energy release rate, crack tip opening displacement, and the critical crack tip opening displacement, respectively. If an unloading of the forces occur during the crack opening, the ECL follows a reversible path connecting the origin with the unloading point on curve $(\Delta_{\max}^*, \bar{t}_{\max})$ with a straight line, where $\bar{t} = \|\bar{\mathbf{t}}\|$, Δ^* , and \bar{t}_{\max} represent the surface traction amplitude between the crack lips, the opening of the crack, and the surface traction amplitude at the maximum crack opening Δ_{\max}^* reached during the fracture process, respectively. The critical opening displacement Δ_c^* is computed, such that $G_c = [(\Delta_c^* \sigma_c)/2]$ is satisfied to ensure that the correct amount of energy is released at the end of the complete fracture process.

In order to couple the DG method with the ECL, let us consider a cracked surface inside the body $\Gamma_C \in \Omega$ in its deformed configuration. The equations (1-3) governing

the strong form are completed in terms of the surface traction $\bar{\mathbf{t}} = \boldsymbol{\sigma} \hat{\mathbf{n}}$ in between two crack lips, where $\boldsymbol{\sigma}$ and $\hat{\mathbf{n}}$ are the Cauchy stress tensor and deformed unit normal outward vector to any of the two lips, respectively. The combination between the fracture modes I and II is obtained as suggested by Camacho and Ortiz [15], and Ortiz and Pandolfi [16] by considering the effective stress σ_{eff} with a fracture criterion as $\sigma_{eff} \geq \sigma_c$, such that

$$\sigma_{eff} = \begin{cases} \sqrt{(\sigma_n)^2 + (\beta)^{-2}(\tau_r)^2}, & \text{if } \sigma_n \geq 0 \\ \frac{1}{\beta} \ll |\tau_r| - \mu_c |\sigma_n| \gg, & \text{if } \sigma_n < 0 \end{cases} \quad (7)$$

where $\beta = (K_{IIC}/K_{IC})$ and μ_c are shear stress factor and friction coefficient of the material, respectively, and where

$$\ll \bullet \gg = \begin{cases} \bullet, & \text{if } \bullet \geq 0 \\ 0, & \text{if } \bullet < 0 \end{cases} \quad (8)$$

In Equation (7), $\sigma_n = \bar{\mathbf{t}} \cdot \hat{\mathbf{n}}$ and $\tau_r = \sqrt{\|\bar{\mathbf{t}}\|^2 - (\sigma_n)^2}$ are respectively the normal and tangential components of the surface traction vector $\bar{\mathbf{t}}$ at the interface. The Cauchy stress tensor $\boldsymbol{\sigma}$ is computed at each interface Gauss quadrature point through the material constitutive law till the fracture criterion, $\sigma_{eff} \geq \sigma_c$, is reached. Once the fracture is detected at a specific interface node, the ECL is used to compute the traction vector $\bar{\mathbf{t}}$ between the two crack lips in terms of the effective opening displacement Δ^* . The effective opening displacement Δ^* is computed from the surface opening vector $\mathbf{\Delta}^*$, which is a combination of two effective openings Δ_n^* and Δ_t^* as given by

$$\Delta^* = \sqrt{\ll \Delta_n^* \gg^2 + \beta^2 (\Delta_t^*)^2} \quad (9)$$

where Δ_n^* and Δ_t^* are the separations along the normal $\hat{\mathbf{n}}$ and tangential $\hat{\mathbf{t}}$ directions, respectively, of the interface element in the deformed configuration. The computation of Δ^* is explained in details by Wu *et al.* [19]. The amplitude of the effective cohesive traction, shown in Figure 2, can then be computed by linear interpolation as

$$\bar{t} = \sigma_c \left(1 - \frac{\Delta^*}{\Delta_c^*}\right) \quad \text{for } \Delta^* \geq 0, \text{ and } \Delta^* = \Delta_{\max}^* \quad (10)$$

$$\bar{t} = \bar{t}_{\max} \frac{\Delta^*}{\Delta_{\max}^*} \quad \text{for } \Delta^* < 0, \text{ or } \Delta^* < \Delta_{\max}^* \quad (11)$$

whereas the cohesive traction vector $\bar{\mathbf{t}}$ can be evaluated as a function of the effective cohesive traction \bar{t} , following

$$\bar{\mathbf{t}} = \bar{t} \left(\frac{\Delta_n^*}{\Delta^*} \hat{\mathbf{n}} + \beta \frac{|\Delta_t^*|}{\Delta^*} \hat{\mathbf{t}} \right) \quad \text{for } \sigma_n \geq 0 \quad (12)$$

$$\bar{\mathbf{t}} = \bar{t} \beta \frac{|\Delta_t^*|}{\Delta^*} \hat{\mathbf{t}} \quad \text{for } \sigma_n < 0 \quad (13)$$

In the DG framework described earlier, the DG surface terms are integrated by the interface elements and the onset of fracture can be detected by the use of a fracture stress criterion as in the ECL approach. When a crack nucleates at a specific node located on an interface element, the DG terms are substituted by the ECL term, which models the fracture process. Hence, if $\bar{\mathbf{t}}^-$ is the surface traction evaluated on the minus

side, the weak form given in Equation (6) that was holding for the bodies without the cracked surfaces only, is modified by the ECL in the deformed configuration to become in the more general situation

$$\left. \begin{aligned} & \int_{\Omega} (\rho \ddot{\mathbf{u}} \cdot \mathbf{w}_u + \boldsymbol{\sigma} : \nabla \mathbf{w}_u) dv + \int_{\Gamma_1} \alpha \bar{\mathbf{t}}^- ([[\mathbf{u}]]) \cdot [[\mathbf{w}_u]] ds + \\ & \int_{\Gamma_1} (1 - \alpha) [[\mathbf{w}_u]] \cdot \langle \boldsymbol{\sigma} \rangle \cdot \hat{\mathbf{n}}^- ds + \\ & \int_{\Gamma_1} (1 - \alpha) [[\mathbf{u}]] \cdot \langle \mathbf{C} : \nabla \mathbf{w}_u \rangle \cdot \hat{\mathbf{n}}^- ds + \\ & \int_{\Gamma_1} (1 - \alpha) [[\mathbf{w}_u]] \otimes \hat{\mathbf{n}}^- : \left\langle \frac{\beta_s}{h_s} \mathbf{C} \right\rangle : [[\mathbf{u}]] \otimes \hat{\mathbf{n}}^- ds = \\ & \int_{\Omega} \rho \mathbf{b} \cdot \mathbf{w}_u dv + \int_{\Gamma_T} \mathbf{w}_u \cdot \bar{\mathbf{t}} ds \end{aligned} \right\} \quad (14)$$

where a binary operator α is defined as $\alpha = 0$ before the fracture onset and $\alpha = 1$ after the fracture stress criterion is met on Γ_1 [17]. All the integration terms are computed in the current configuration for the small deformations. Unlike for the intrinsic CZM, no modification of the mesh is required during the shift procedure from the uncracked ($\alpha = 0$) to cracked ($\alpha = 1$) configuration, and only the constitutive formulations at the interface elements are modified, thus implicitly treating an interface element as a cohesive element. This makes the hybrid DG/ECL method easy to be implemented in an existing parallel code, and ensures a high scalability of the parallel simulations.

The σ_c and G_c are the two minimum parameters required for the characterisation of the ECL. In this work, we will evaluate these values at the macroscopic scale, where the material is considered as isotropic and homogeneous from the micro-scale simulations. At the microscopic scale (through mesoscopic RVE) we develop a method accounting for the anisotropy and heterogeneity of the polySi caused due to the different out of plane orientation of the grains.

3 Microscale fracture of RVE mode of polySi material

At first, we study the RVE of polySi at the mesoscopic (microscopic) scale with several grains. A completely general distribution of grains is considered, such that the simulated volume can be assumed to be a RVE. The values of effective σ_c and G_c are evaluated at the mesoscopic scale by accounting for the anisotropic and heterogeneous nature of the polySi due to a general out-of-plane orientation of grains. Thus, the effective values are at first computed for a general orientation of grains, and secondly the weakest plane is identified over the thickness of a thin polySi film for the through-the-thickness fracture such that the correct amount of energy is released at the end of the fracture.

3.1 Effective fracture strength

At first, the effective σ_c and G_c values are computed along the interface elements present in the discretized RVE at the mesoscopic length scale. The length of a single interface element is several times larger than the single crystal lattice spacing of polySi. Thus, the approach presented here to compute the values of effective σ_c and G_c is valid for a certain ‘‘average’’ direction (out-of-plane orientation) of a grain.

The polySi is an orthotropic material, i.e., it has different material properties, such as Young’s modulus, Poisson’s ratio, fracture strength, along the crystal planes with

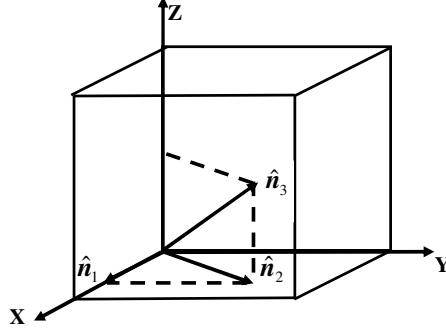


Figure 3: Symmetry-equivalent surfaces with their normals

Miller indices (1 0 0), (1 1 0), and (1 1 1), shown in Figure 3 as \hat{n}_1 , \hat{n}_2 , and \hat{n}_3 , respectively. The surface normal of the 2D interface (cohesive) elements, located in-between two bulk elements, in a discretized model are not exactly aligned with any of the surface normals shown in Figure 3. Thus, a suitable model is warranted that computes σ_c based on the orientation of the cohesive element with respect to the surface normals shown in Figure 3. For a cubic crystal, the Miller indices (hkl) are normal to the surface vector $[hkl]$, i.e., Miller indices directly give the coefficients of the surface normal vector for a cubic crystal. Thus, this information allows obtaining the effective σ_c for any random orientation of a polySi grain as explained further. The same approach is also applied to compute the effective G_c .

In the case of a single crystal silicon, the values of the fracture strength are experimentally measured along the three possible cleavage planes (1 0 0), (1 1 0), and (1 1 1) [2, 20, 21]. Let these values be σ_{100} , σ_{110} , and σ_{111} , respectively. The normal vectors to these planes are given as $\hat{n}_1 = \hat{e}_1$, $\hat{n}_2 = (1/\sqrt{2})(\hat{e}_1 + \hat{e}_2)$, and $\hat{n}_3 = (1/\sqrt{3})(\hat{e}_1 + \hat{e}_2 + \hat{e}_3)$, respectively, where \hat{e}_i are the unit basis vectors of the global Cartesian axes as shown in Figure 3. Let there be an interface (cohesive) element, having a surface normal vector \vec{n} , along which σ_c has to be determined.

The surface normal vector \vec{n} can be represented in the contravariant form as $\vec{n} = n^i \hat{n}_i$, where the \hat{n}_i are treated as the local basis vectors. As the vectors \hat{n}_1 , \hat{n}_2 , and \hat{n}_3 are not orthogonal to one another, their dual vectors are computed at first. The total volume contained within the local basis vectors is

$$v = (\hat{n}_1 \times \hat{n}_2) \cdot \hat{n}_3 \Rightarrow v = \frac{1}{\sqrt{6}} \quad (15)$$

The dual basis vectors are then computed as

$$\left. \begin{aligned} \vec{n}^1 &= \left[\frac{\hat{n}_2 \times \hat{n}_3}{v} \right] \Rightarrow \vec{n}^1 = \hat{e}_1 - \hat{e}_2 \\ \vec{n}^2 &= \sqrt{2}(\hat{e}_2 - \hat{e}_3), \text{ and } \vec{n}^3 = \sqrt{3}\hat{e}_3 \end{aligned} \right\} \quad (16)$$

such that $\vec{n}_i \bullet \vec{n}^j = \delta_i^j$ is satisfied. The projection of \vec{n} in the dual basis vectors is given as

$$n^{100} = \vec{n} \cdot \vec{n}^1, \quad n^{110} = \vec{n} \cdot \vec{n}^2, \quad n^{111} = \vec{n} \cdot \vec{n}^3 \quad (17)$$

Therefore, the effective fracture strength vector $\boldsymbol{\sigma}_c$ along \vec{n} can be constructed as

$$\begin{aligned}\boldsymbol{\sigma}_c &= \sigma_{100} n^{100} \hat{\mathbf{n}}_1 + \sigma_{110} n^{110} \hat{\mathbf{n}}_2 + \sigma_{111} n^{111} \hat{\mathbf{n}}_3 \Rightarrow \\ &= \left(\sigma_{100} n^{100} + \frac{\sigma_{110} n^{110}}{\sqrt{2}} + \frac{\sigma_{111} n^{111}}{\sqrt{3}} \right) \hat{\mathbf{e}}_1 + \\ &\quad \left(\frac{\sigma_{110} n^{110}}{\sqrt{2}} + \frac{\sigma_{111} n^{111}}{\sqrt{3}} \right) \hat{\mathbf{e}}_2 + \left(\frac{\sigma_{111} n^{111}}{\sqrt{3}} \right) \hat{\mathbf{e}}_3\end{aligned}\quad (18)$$

The magnitude σ_c of $\boldsymbol{\sigma}_c$ is thus given as

$$\sigma_c = \sqrt{\left(\sigma_{100} n^{100} + \frac{\sigma_{110} n^{110}}{\sqrt{2}} + \frac{\sigma_{111} n^{111}}{\sqrt{3}} \right)^2 + \left(\frac{\sigma_{110} n^{110}}{\sqrt{2}} + \frac{\sigma_{111} n^{111}}{\sqrt{3}} \right)^2 + \left(\frac{\sigma_{111} n^{111}}{\sqrt{3}} \right)^2}\quad (19)$$

This equation is applicable only when \vec{n} is in between the solid angle formed by $\hat{\mathbf{n}}_1$, $\hat{\mathbf{n}}_2$, and $\hat{\mathbf{n}}_3$, where these are the surface normal vectors corresponding to the orientation planes (1 0 0), (1 1 0), and (1 1 1), respectively, which may not always be true. The symmetry property of the cubic crystal is used to enable the applicability of Eq. (19). Due to the symmetry of the cubic crystal, there are 26 symmetry planes distributed in 8 quadrants as

$$\left. \begin{aligned}\{100\} &= (100), (010), (001), (\bar{1}00), (0\bar{1}0), (00\bar{1}) \\ \{110\} &= (110), (\bar{1}10), (\bar{1}\bar{1}0), (\bar{1}\bar{1}0), (011), (0\bar{1}1), \\ &\quad (0\bar{1}\bar{1}), (101), (10\bar{1}), (\bar{1}0\bar{1}), (\bar{1}01), (01\bar{1}) \\ \{111\} &= (111), (\bar{1}11), (\bar{1}\bar{1}1), (\bar{1}\bar{1}1), (11\bar{1}), (\bar{1}1\bar{1}), \\ &\quad (\bar{1}\bar{1}\bar{1}), (1\bar{1}\bar{1})\end{aligned}\right\} \quad (20)$$

The magnitude of the fracture strength is equal along all the planes within each family of planes $\{100\}$, $\{110\}$, and $\{111\}$. These symmetry planes (26) give a total of 48 sets of the solid angles (6 solid angles per quadrant). This information is used while determining the correct solid angle in which the vector \vec{n} lies. At first, each set of the solid angle is considered, and the corresponding dual basis vectors are computed. The vector \vec{n} is then projected in these dual basis vectors. If all the projections are ≥ 0 for a specific solid angle, it is concluded that the vector \vec{n} lies within this solid angle formed by the set of 3 corresponding surface normal vectors. Finally, the correctly identified set of the surface normal vectors is used while computing the effective σ_c along the plane normal to the vector \vec{n} , as given in Equation (19). In order to test the correctness of Eq. (19), the Cartesian coordinates of \vec{n} are constructed by the polar coordinates (by progressively increasing the angles $\theta \in [0, 2\pi]$ and $\phi \in [0, \pi]$), and the corresponding effective σ_c is computed by Eq. (19). The results are presented in Figure 4 for specific values $\sigma_{100} = 1.53$, $\sigma_{110} = 1.21$, and $\sigma_{111} = 0.868$ GPa of a single crystal silicon [2, 20, 21]. It can be seen that the effective σ_c passes through the three values used along the symmetry planes with the symmetric distribution in all the 8 quadrants of a unit length cubic crystal, which is an expected result. This model is also applied to compute the $G_{c_{eff}}$ along the interface plane with surface normal \vec{n} as shown in Figure 5.

3.2 Thickness effect

The fracture process of a thin polySi film is currently modeled as a 2D plane-stress problem, thus the surface normal vector \vec{n} of the cohesive element always lies in the

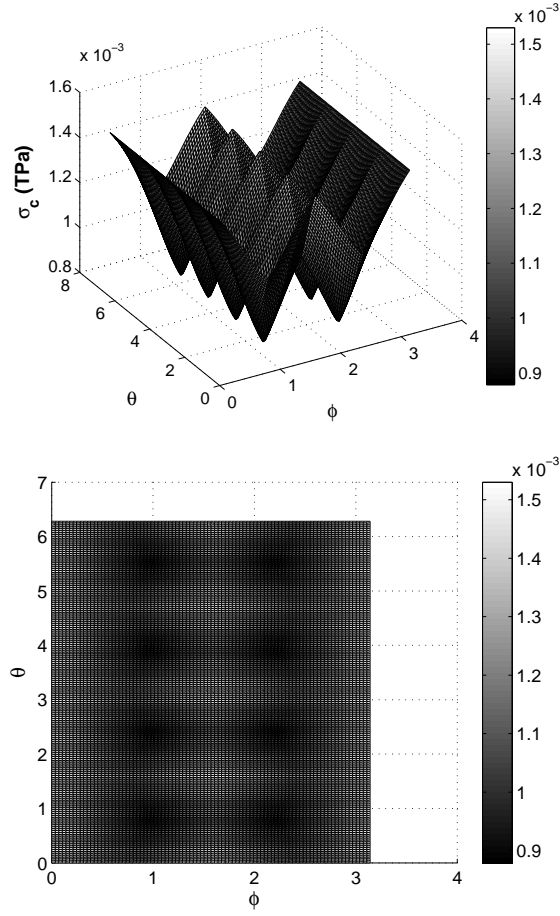


Figure 4: Distribution of σ_c within a unit cube of polycrystalline silicon

plane. It is in reality a 3D problem, as several grains are experimentally observed along the thickness of a thin polySi film. Thus, the fracture surface normal $\hat{\mathbf{n}}$ may be oriented with a certain angle along the thickness of the film, where the effective value of σ_c could be lower as compared with the plane-stress situation. The following approach, as shown in Figure 6 where $\hat{\mathbf{n}} \equiv \hat{\mathbf{n}}$, is thus adopted to incorporate this aspect in order to account for 3D nature of the problem.

Let us assume an interface (cohesive) element, and let $\hat{\mathbf{t}}, \hat{\mathbf{t}}_0$, and $\hat{\mathbf{n}}$ be the in-plane surface tangent, surface tangent, and out-of-plane surface normal vectors, respectively, as shown in Figure 6. These 3 vectors form a set of local basis vectors, and the Cauchy stress tensor $\boldsymbol{\sigma}$ is represented in terms of these local basis vectors. This interface element is now rotated by an angle θ about $\hat{\mathbf{t}}$. Thus, the local basis vectors transform to $\hat{\mathbf{t}}', \hat{\mathbf{t}}'_0$, and $\hat{\mathbf{n}}'$, respectively. The transformation equations are given as

$$\left. \begin{aligned} \hat{\mathbf{n}}' &= \cos(\theta) \hat{\mathbf{n}} + \sin(\theta) \hat{\mathbf{t}}_0 \\ \hat{\mathbf{t}}' &= \hat{\mathbf{t}} \\ \hat{\mathbf{t}}'_0 &= -\sin(\theta) \hat{\mathbf{n}} + \cos(\theta) \hat{\mathbf{t}}_0 \end{aligned} \right\} \quad (21)$$

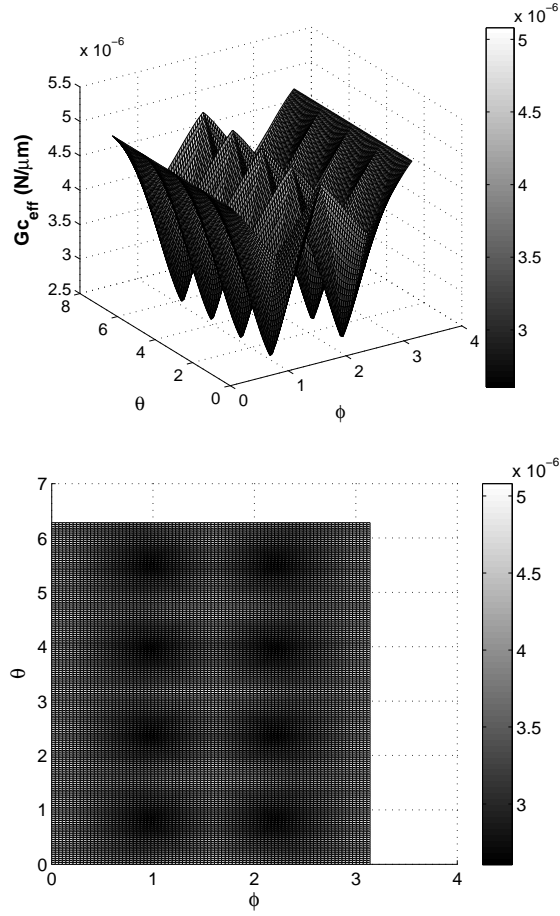


Figure 5: Distribution of G_c within a unit cube of polycrystalline silicon

The Cauchy stress tensor $\boldsymbol{\sigma}$ is already available along the interface element. Also the effective values of $\sigma_c(\theta)$ and $G_{c_{eff}}(\theta)$ are computed in the direction $\hat{\mathbf{n}}'$, as explained in Section 3.1. Now, the magnitude of the stresses acting on the rotated plane are computed from $\boldsymbol{\sigma}$ and $\hat{\mathbf{n}}'$, $\hat{\mathbf{i}}'_0$, and $\hat{\mathbf{j}}'_0$ as

$$\left. \begin{aligned} \sigma_n &= (\boldsymbol{\sigma} \hat{\mathbf{n}}') \cdot \hat{\mathbf{n}}', \tau = (\boldsymbol{\sigma} \hat{\mathbf{n}}') \cdot \hat{\mathbf{i}}', \tau_0 = (\boldsymbol{\sigma} \hat{\mathbf{n}}') \cdot \hat{\mathbf{j}}'_0 \\ \tau_r &= \sqrt{(\tau)^2 + (\tau_0)^2} \end{aligned} \right\} \quad (22)$$

The effective stress $\sigma_{eff}(\theta)$ along the rotated plane is computed from σ_n and τ_r using Equation (7). The $\sigma_c(\theta)$, $G_{c_{eff}}(\theta)$, and $\sigma_{eff}(\theta)$ are computed with θ varying from -90° to $+90^\circ$ with a fixed increment. If the fracture criterion $\sigma_{eff}(\theta) \geq \sigma_c(\theta)$ is satisfied, $\alpha = 1$ is used in Equation (14). This $\sigma_{eff}(\theta)$ value is used to compute the maximum effective crack tip opening $\Delta_c^*(\theta) = (2G_{c_{eff}}(\theta)/\sigma_{eff}(\theta))$. The in-plane crack tip opening is computed as $\Delta^* = \{\Delta_c^*(\theta)/\cos(\theta)\}$, such that the correct amount of energy is released by ECL method. The $\sigma_{eff}(\theta)$ value corresponding to $\theta = 0$ is used in the cohesive law, shown in Figure 2, as a starting point ($\Delta^* = 0, \sigma_c$) in order to maintain the

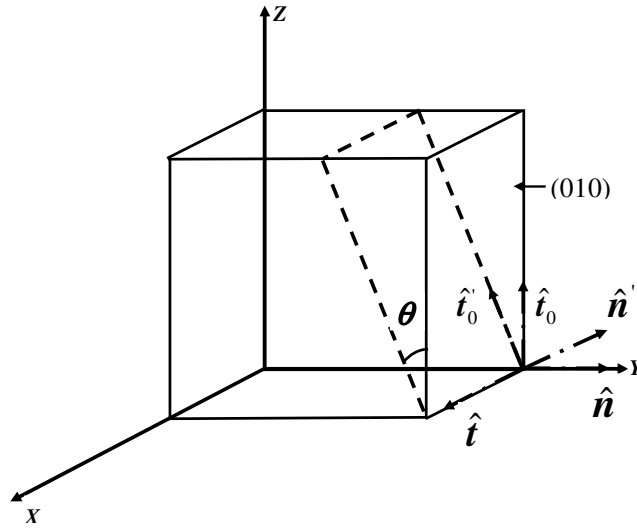


Figure 6: Rotation of an interface element along the thickness of the thin polySi film, where \hat{n} is shown along Y axis for an illustration purpose.

continuity of the distribution of the stress field between the unfractured and fractured stages.

3.3 Results and discussion

The 2-D plane-stress type modelling and simulation of the fracture of a thin polySi film RVE is performed as follows. At first, a model of a thin polySi film is developed by Voronoï tessellation with each Voronoï polygon treated as a grain. The size of each grain is approximately maintained equal to 100 nm, and a random orientation (random Euler angles) is assigned as shown in Figure 7a. However, the preferential orientations as experimentally observed can also be assigned as demonstrated in Section 3.3.2. The dimensions of the model are chosen such that a stable fracture process can be obtained, i.e., the total strain energy stored in a body should be less than or equal to the total fracture energy required to be released. The following approach has been followed to satisfy this requirement. At first, the dimensions of the model are fixed with certain length l , height h and thickness t , and one sample simulation is performed by an appropriate value of the load step that approximately gives a quasi static loading. Based on the microscopic stress vs strain plot obtained at the end of the simulation, the correct length of the model is computed by $l \leq (G_c / (0.5 \sigma_c \epsilon_c))$, where G_c , σ_c and ϵ_c are the critical strain energy release rate, obtained fracture stress and strain, respectively. The model is then regenerated with this new value of length l to approximately ensure that the stable through-the-thickness fracture is obtained, such that the total fracture energy to be released is approximately equal to $(G_c ht)$, where h and t are the height and thickness of the model, respectively. The typical finite element mesh size is decided with reference to the smallest edge of the grains present in a model as shown in Figure 7b. This ensures that at least one element is present along the grain boundaries.

This model is clamped at one end and pulled at the other end. The force (computed) and displacement (applied) values along the loading edge are archived. The

dynamic explicit time integration is performed to ensure convergence, and the value of the load step is decided to ensure that almost the quasi-static simulation is achieved. The interelement boundaries are treated as interface elements in the DG method, and interior domain of elements is treated as a bulk domain. Thus, the interface terms of the weak form of DG formulation, as given in Eq. (14), are applied only over the interface elements, as the discontinuities are allowed across the interelement boundaries. As soon as a fracture is detected at any node along the interface element, the monotonically decreasing linear ECL is applied to compute the stress. The interface elements are present at two locations, viz. within a grain and along the grain boundaries. The fracture strength and effective stress along the interface elements, that are present within a grain, are computed as explained in Sections 3.1 and 3.2, respectively. The value of fracture strength along the interface elements, that are present along the grain boundaries, is assigned corresponding to the (1 0 0) orientation, and the effective stress is computed without the thickness effect. This adopted approach in the present work is based on the experimentally observed fact that the polySi mainly undergoes the transgranular fracture, so the grain boundaries are stronger than the grains.

In order to capture the spread of fracture strength associated to the orientation of grains, 10 different sets of the fracture results are obtained with each time new Euler angles assigned to the grains. For each of the 10 sets, a macroscopic ECL is extracted from the microscopic force vs. displacement plot [18, 19], as $u^M = u^m - [(l/E)(f^m/(ht))]$ where f^m , u^m and u^M are the microscopic force, displacement and macroscopic displacement, respectively, and E is the slope of microscopic stress vs. strain plot till the fracture stress is reached. The mean and standard deviation of the macroscopic effective crack tip opening displacement Δ^* and fracture stress σ_c are computed based on the 10 sets of the extracted macroscopic ECL from the simulation results. An average macroscopic cohesive law is thus developed that incorporates the statistical variation of σ_c and Δ^* . Secondly, a new model of the thin polySi film is chosen to perform the simulation at the macroscopic or MEMS length scale where the domain of the model is treated as continuum, i.e., without the underlying microstructure. The average macroscopic cohesive law is imposed, for the nodes where the fracture is detected, by specifying the values of σ_c and G_c at each node within their lower and upper limits, such that the effective macroscopic opening Δ^* is obtained within its upper and lower limits. All the simulation results are finally compared with several experiments in the subsequent sections. The simulation at the macroscopic scale implicitly assumes that the underlying microstructure of the MEMS is closely represented by the RVE at the mesoscopic length scale, such that the statistical variation of the fracture strength obtained by the RVE closely represents the actual scenario at the MEMS length scale.

3.3.1 Fracture of a thin polySi film RVE at microscopic level

At first, a microscopic model of a thin polySi film RVE is developed by Voronoi tessellation as shown in Figure 7, where the grains are represented by Voronoi polygons. The average size of grains is maintained as ≈ 100 nm, and the dimensions of the model are $l = 1.15$, $h = 1$ and $t = 0.05$ μm . The values of the load step and the size of the finite element are decided, as explained earlier, to ensure that the stable fracture is obtained. Experimentally, the fracture strength of a single crystal silicon is highly affected by the micromachining process and the silicon etchant used, thus a wide variation is observed in its value [2, 20]. It is little difficult to exactly incorporate the actual surface quality of a thin polySi film in the present simulation. The standard values for typical silicon

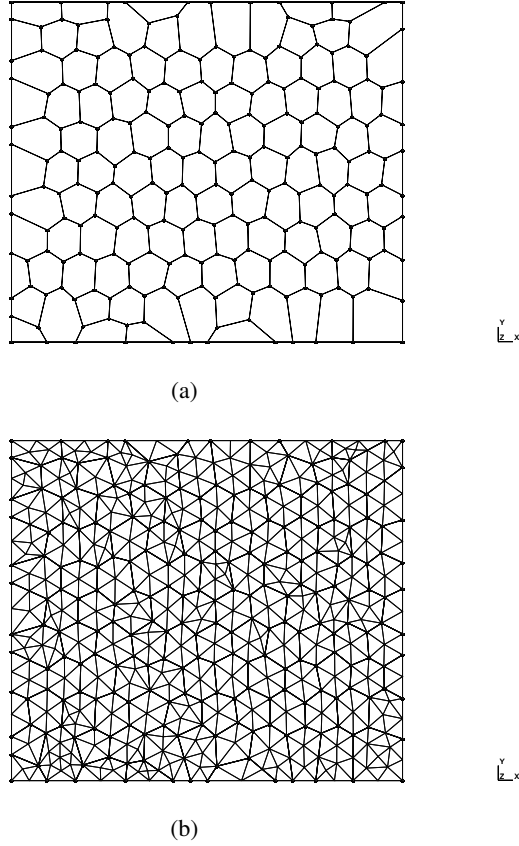


Figure 7: A representative volume element model of a thin polySi film with (a) 112 grains and (b) a mesh containing 874 elements

crystals produced by the most common micromachining process are used in the present study. The values of fracture strength along the (1 0 0), (1 1 0) and (1 1 1) orientation planes for the single crystal silicon are used as $\sigma_{100} = 1.53 \times 10^{-3}$, $\sigma_{110} = 1.21 \times 10^{-3}$ and $\sigma_{111} = 0.868 \times 10^{-3}$ TPa [2, 20, 21], respectively. The values of Gc are similarly used as $Gc_{100} = 5.08 \times 10^{-6}$, $Gc_{110} = 4.2 \times 10^{-6}$ and $Gc_{111} = 2.56 \times 10^{-6}$ N/ μm , [22,23], respectively. In order to ensure that the fracture is preferably detected at a single location at the beginning, the computed value of the effective fracture strength at a specific Gauss point along the interface element is varied within $\pm 10\%$. The Young's modulus $E = 144 \times 10^{-3}$ TPa is used, which correspond to the single crystal silicon having a preferential (1 0 0) orientation [2, 20, 21, 24]. The values of the density and Poisson's ratio of the polySi are $\rho = 2.33 \times 10^{-21}$ KiloTonne/ μm^3 and $\nu = 0.278$, respectively. An anisotropic Hooke's law is applied to relate the stress with the strain. Different sets (10) of the fracture results are now obtained for this model by each time assigning a random out-of-plane orientation to the grains.

The results from one of the sets are provided here for a reference. The random out-of-plane orientation of 112 grains is shown by the stereographic projection of the surface normal of their orientations in Figure 8. There is no preferential out-of-plane orientation in this case. The microscopic stress vs. strain plot is shown in Figure 9a,

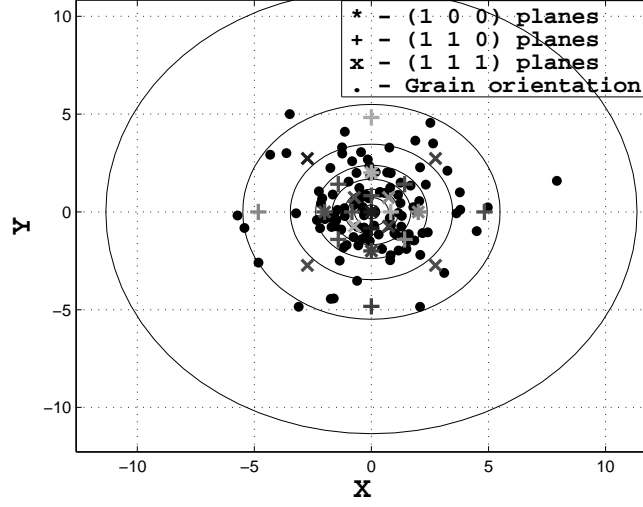


Figure 8: Stereographic projection of the surface normal of the orientation of grains without any average preferred orientation

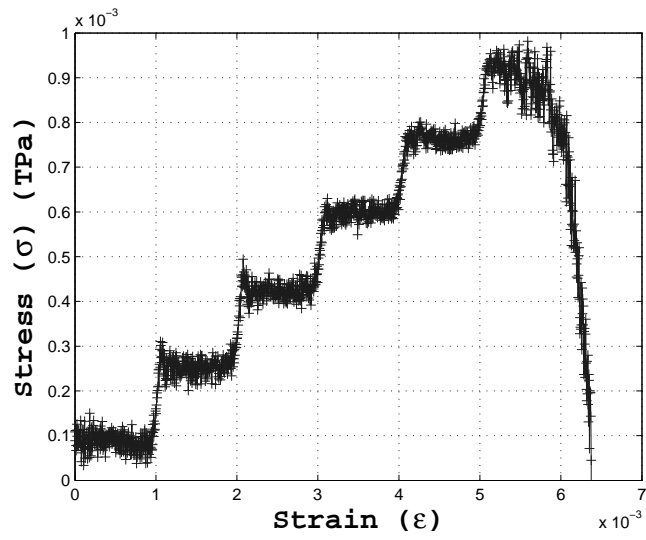
and the extracted macroscopic cohesive law is shown in Figure 9b. The through-the-thickness fracture is shown in Figure 9c. The external load steps could be seen in Figure 9a for the pre-fracture state that are caused by the dynamic effects. The smooth loading can be obtained by further reducing the time step, but it may lead to a non-physical situation where multiple cracks are detected at the same time. It is also seen in Figure 9c that the crack is initiated at both ends of the polySi RVE. This could be explained by the fact that no notches are present along the edges, so there is an equal probability of the crack occurring at several places, along the height of the model, at the same time. The more important aspects are that both cracks finally meet, and that fracture is transgranular. Few elements could be disturbed during the crack propagation, as there is no stress concentration at the onset of crack so the fracture may be detected at more than one nodes along the interface elements belonging to the same bulk element. The effective $G_c = (0.5 \Delta_c^* \sigma_c)$ is computed by the macroscopic cohesive law given in Figure 9b and obtained as $G_c = 2.97 \times 10^{-6} \text{ N}/\mu\text{m}$, where $\Delta_c^* = 5.6 \times 10^{-3} \mu\text{m}$ and $\sigma_c = 1.0 \times 10^{-3} \text{ TPa}$.

The results obtained by all the 10 simulated sets are analyzed, as explained above, and one macroscopic cohesive law is extracted for each realization. Because of the random nature of the grain orientation, each realisation leads to the different values of σ_c and G_c . The values of mean $\bar{\sigma}_c$ and standard deviation σ_{σ_c} of σ_c are computed as

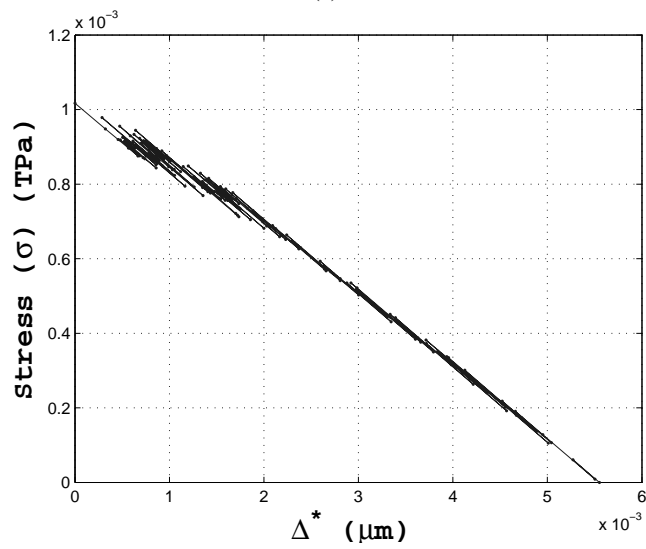
$$\bar{\sigma}_c = \frac{1}{n} \sum_{i=1}^n (\sigma_c)_i, \quad \sigma_{\sigma_c} = \sqrt{\frac{1}{(n-1)} \sum_{i=1}^n [(\sigma_c)_i - \bar{\sigma}_c]^2} \quad (23)$$

where $n = 10$ is our sample size. the values of mean $\bar{\Delta}_c^*$ and standard deviation $\sigma_{\Delta_c^*}$ of Δ_c^* are also computed similarly. These values are obtained as $\bar{\sigma}_c = 0.99 \times 10^{-3} \text{ TPa}$ and $\sigma_{\sigma_c} = 4.04 \times 10^{-5} \text{ TPa}$, and $\bar{\Delta}_c^* = 5.98 \times 10^{-3} \mu\text{m}$ and $\sigma_{\Delta_c^*} = 4.96 \times 10^{-4} \mu\text{m}$. The average macroscopic cohesive law is thus developed based on these values as shown in Figure 11. It is to be noted that these values are linked with the size of the polySi RVE, and will change with a change in the size of the RVE [25, 26].

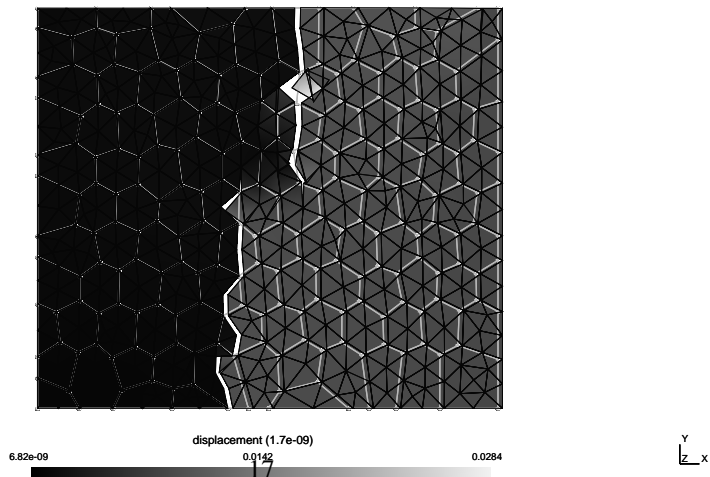
All the simulation results at the microscopic level show that the first fracture always



(a)



(b)



(c)

Figure 9: (a) Stress vs. strain plot of microstructure, (b) macroscopic cohesive law, (c) through-the-thickness fracture when the grains in a thin polySi film are assigned a random orientation

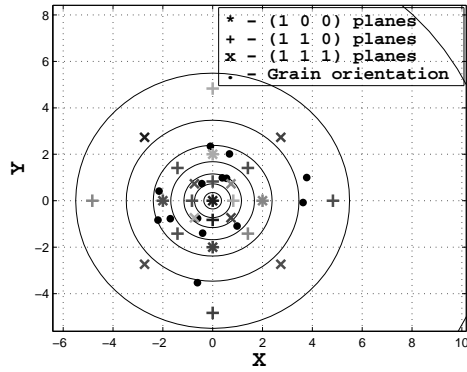


Figure 10: Stereographic projection of the surface normal of the out-of-plane orientation of grains that are involved in the fracture process shown in Figure 9c, where an average preferred orientation is in between (1 1 0) and (1 1 1)

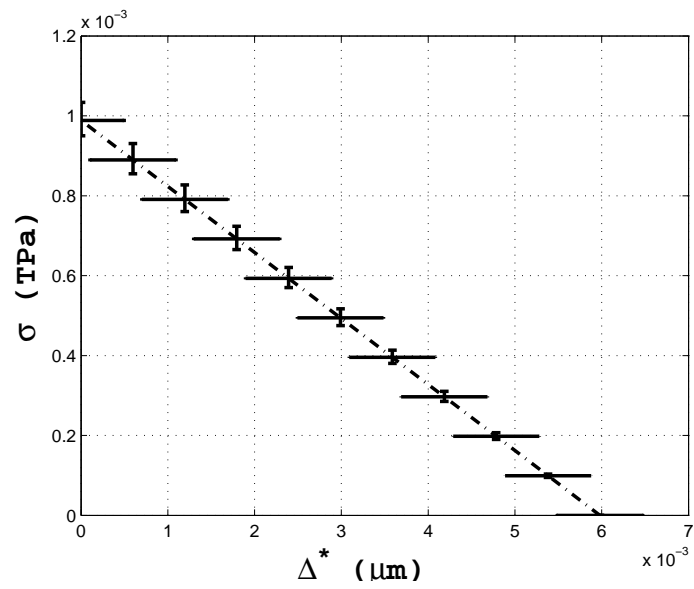


Figure 11: Average macroscopic extrinsic cohesive law

occurs at the value of effective stress $\sigma_{eff}(\theta)$, as explained in Section 3.2, in between the fracture strengths along the (1 1 0) and (1 1 1) orientation planes. This means that, irrespective of the orientation of grains, there will be at least one interface element whose surface normal will be closely aligned, due to the thickness effect, to the surface normal of the plane with out-of-plane (1 1 1) orientation. This implies that the crack will always propagate in the average direction of out-of-plane (1 1 1) orientation. This is clearly seen in Figure 10, where the stereographic projection is given only for the grains that are involved in the fracture process where an average preferred out of plane orientation is in between the (1 1 0) and (1 1 1) orientations. A similar behaviour has also been experimentally observed [23]. The average value of $G_c \approx 2.96 \times 10^{-6} \text{ N}/\mu\text{m}$ is also in between the values corresponding to the (1 1 0) and (1 1 1) orientation planes. All the results at microscopic level have different crack paths, as each time different out of plane orientation is assigned to the grains. The orientation of grains thus does affect the crack path, while may not drastically affect the fracture stress at which crack initiation is detected.

3.3.2 Fracture of a thin polySi film RVE with grain orientations close to (1 1 0)

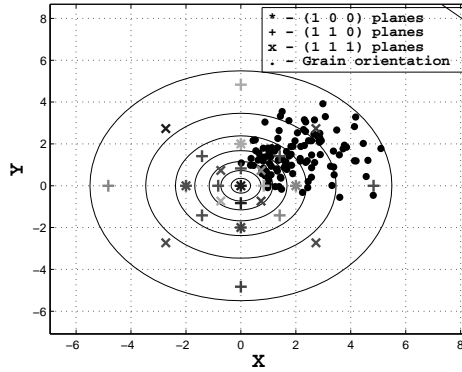
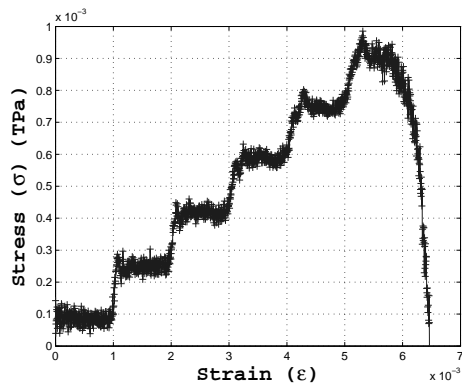


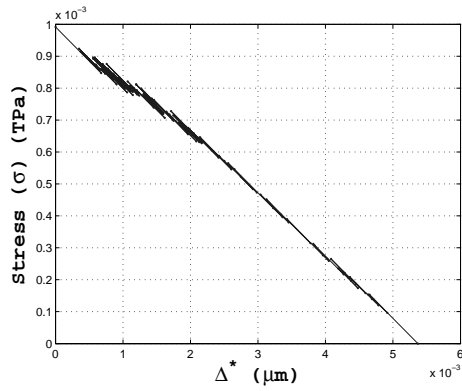
Figure 12: Stereographic projection of the surface normal of the orientation of grains with an average (1 1 0) orientation

This section contains the simulation results when all the grains in Figure 7a are assigned an out of plane orientation close to (1 1 0) plane. The objective of this simulation is to make comparisons with several experimental results in the open literature, as well as in-house experiments performed as explained later. All the material properties as well as the parameter values are the same as explained earlier. The average (1 1 0) orientation of grains is shown by their stereographic projection in Figure 12. The microscopic stress vs. strain plot and the macroscopic cohesive law are shown in Figures 13a and 13b, respectively, and the crack path is shown in Figure 14. The value of effective G_c is computed by the cohesive law as well as energy balance as equal to 2.77×10^{-6} and $3.0 \times 10^{-6} \text{ N}/\mu\text{m}$, respectively. These values are approximated as they are computed by assuming a complete mode-I fracture, such that the fracture surface area is assumed to be a normal cross-section ($h \times t$). The crack path where as shows that the actual fracture surface is not exactly along the normal cross-section.

The fracture strength obtained is equal to $\sigma_c \approx 1.0 \times 10^{-3} \text{ TPa}$, which is close to the average value obtained by Yi *et al.* [20] but slightly lower than the input value $\sigma_{110} = 1.21 \times 10^{-3} \text{ TPa}$ for a single crystal silicon with a preferred (1 1 0) out-of-plane

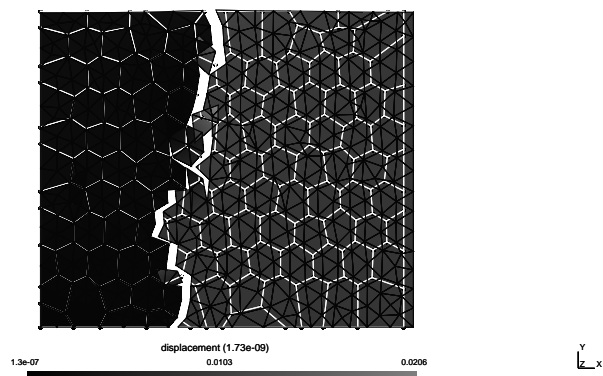


(a)



(b)

Figure 13: (a) Stress vs. strain plot, (b) macroscopic cohesive law for an average (1 1 0) grain orientation



(a)

Figure 14: Full through-the-thickness fracture for an average out of plane (1 1 0) grain orientation

orientation. The reason behind this was explained at the end of Section 3.3.1. The present results closely match with Suwito *et al.* [2] for $\langle 110 \rangle$ silicon T-structures having sharp 90° corner at the point of the reduction of cross-sectional area. This is an important test case as it mimics the actual transitions that occur in the micromechanical structures. The value of fracture strain is $\epsilon_c \approx 0.56\%$, which is very close to the average value obtained by Sato *et al.* [21] for a single crystal silicon film having $\langle 110 \rangle$ preferred orientation.

Now, the average macroscopic ECL given in Figure 11 is tested by performing the simulation of a thin polySi film at the macroscopic level with a larger model. This macroscopic ECL is implemented by randomly assigning the σ_c and G_c bounded by their lower and upper limits (obtained in Section 3.3.1) at each node, such that the critical crack tip opening displacement Δ_c^* is automatically bounded by its lower and upper limits. Thus, $\sigma_c^- = 0.948 \times 10^{-3}$, $\sigma_c^+ = 1.03 \times 10^{-3}$ TPa, and $G_c^- = 2.8297 \times 10^{-6}$, $G_c^+ = 2.955 \times 10^{-6}$ N/ μm values are used such that $(\Delta_c^*)^- = 5.5 \times 10^{-3}$, $(\Delta_c^*)^+ = 6.5 \times 10^{-3}$ μm values are obtained. The simulation of a thin polySi film at the macroscopic level is illustrated in the subsequent sections by three different models.

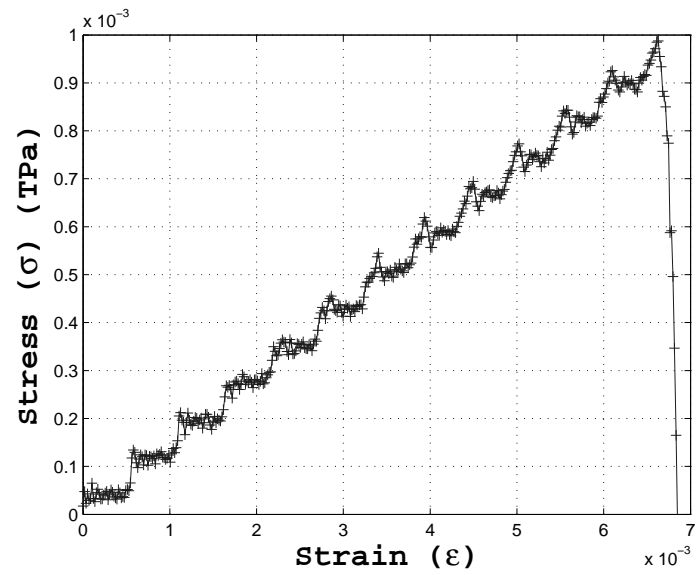
4 Fracture of a thin polySi film at the macroscopic level

The average macroscopic ECL given in Figure 11 is applied to simulate the fracture of a thin polySi film at the macroscopic length scale. Thus, an anisotropic and heterogeneous nature of the microstructure at the mesoscopic length scale is captured by the variation in the values of σ_c and G_c at the macroscopic scale. This is achieved firstly without considering any defect, and secondly with considering an edge defect at the center of the length l of a thin polySi film.

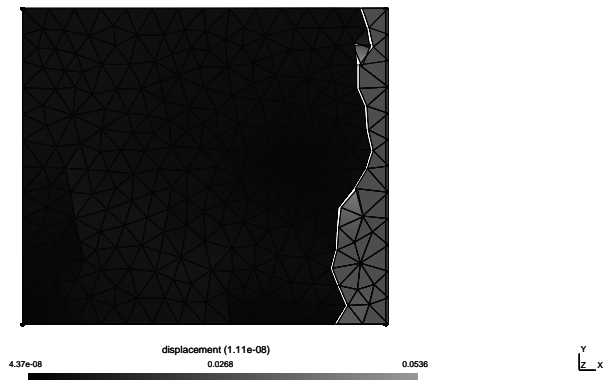
4.1 Fracture of a thin polySi film without any notch at the macroscopic level

A new model is considered with $l = 3.45$, $h = 3$ and $t = 0.05$ μm at the macroscopic length scale. This model is discretized such that the size of the finite elements is approximately equal to the size of the RVE considered in Section 3.3.1. The results of the simulation are as follows. The stress vs. strain plot and the fracture are shown in Figure 15. The total surface or fracture energy for this model $U_{surf} \approx (3.0 \times 0.05 \times 3 \times 10^{-6}) \approx 4.5 \times 10^{-7}$ N- μm is well achieved at the end of the fracture. The fracture in the present case is unstable, evident from Figure 15a, as the total strain energy U_{int} at the beginning of the fracture is much higher than the required fracture energy.

In order to test the correctness of the macroscopic cohesive law as well as DG/ECL framework implementation, the length l is modified, such that the stable fracture is obtained, as explained in Section 3.3. The values of σ_c and ϵ_c are taken from Figure 15a and an average $G_c = 2.9 \times 10^{-6}$ N/ μm is used to compute the new length $l \approx 0.9$ μm . The new model is built again and simulated with all the parameters as before. The simulation results show that a perfect stable mode-I fracture is obtained and all the vital values are correctly recovered. The stress vs. strain plot and the cohesive law are given in Figure 16, and the complete mode-I fracture is given in Figure 16c. The total potential energy at the end of fracture is $U_{pot} = 4.2 \times 10^{-7}$ N- μm , which gives $G_c = 2.799 \times 10^{-6}$ N/ μm for a normal cross-section (3.0×0.05) μm^2 . The total area under the cohesive law also equal to $G_c = 2.977 \times 10^{-6}$ N/ μm . The maximum internal

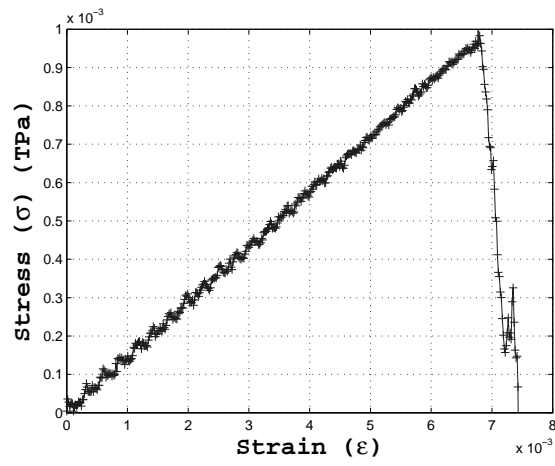


(a)

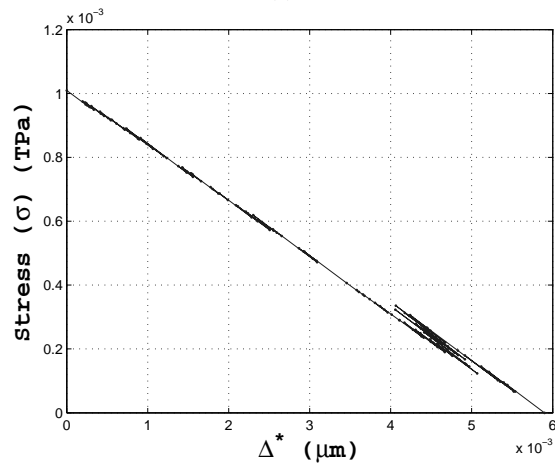


(b)

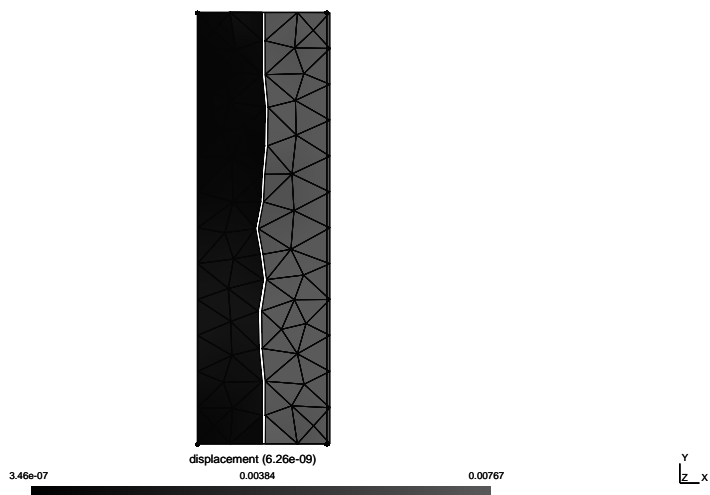
Figure 15: (a) Stress vs. strain plot, (b) complete fracture of a thin polySi film at the macroscopic level for the model discretized by 504 finite elements



(a)



(b)



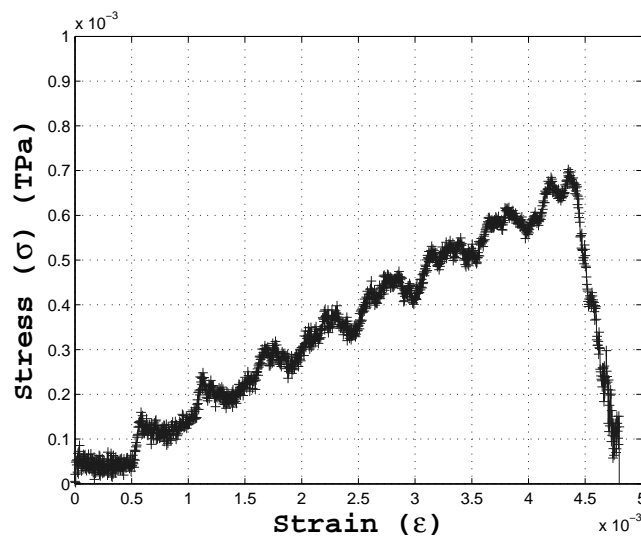
(c)

Figure 16: (a) Stress vs. strain plot, (b) global cohesive law of a thin polySi film, (c) complete mode-I fracture for the stable crack propagation at the macroscopic level

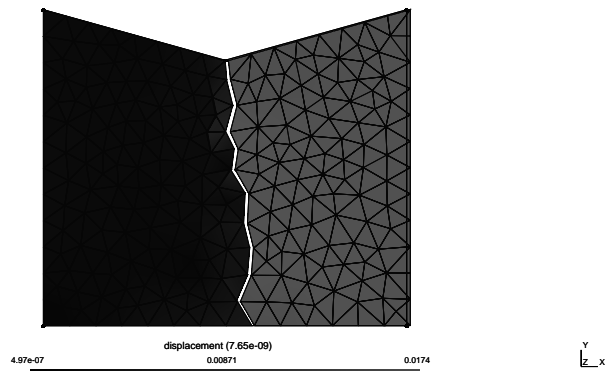
strain energy $U_{int} = 4.37 \times 10^{-7}$ N- μ m, which is close to the total required fracture energy $U_{surf} = 4.5 \times 10^{-7}$ N- μ m, results in a stable crack propagation.

4.2 Fracture of a thin polySi film with an edge defect at the macroscopic level

All the simulation results presented so far correspond to the geometry of a thin polySi film with smooth edges. In reality, several defects (notches) are generated along the edges of MEMS due to the micromachining process, thus considerably affecting the fracture behaviour of MEMS. Thus, it is pertinent to study such a model of a thin polySi film having at least a one edge defect.



(a)

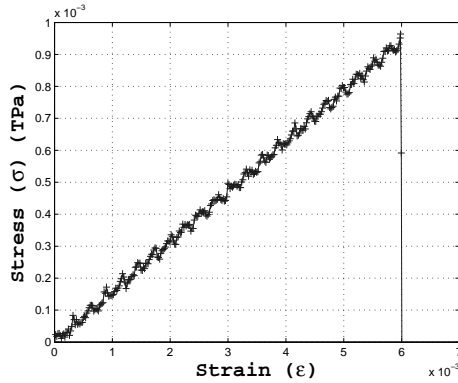


(b)

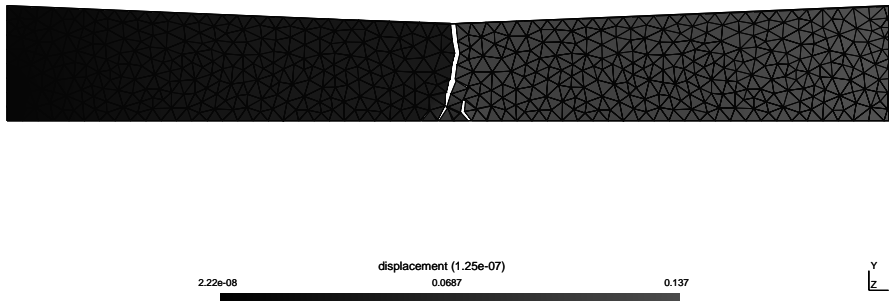
Figure 17: (a) Stress vs. strain plot, and (b) complete fracture of a thin polySi film, having a notch, at the macroscopic level

The macroscopic model from Section 4.1 is modified at first and a defect in the

form of a small notch is created at the centre of a top edge, such that the height at the centre became $h_c = 2.52 \mu\text{m}$. The simulation is performed keeping all the parameters as before. Figures 15a and 17a show that the fracture stress is reduced by at least 20% due to the presence of the defect. The obtained crack path can also be physically observed as there will be a stress concentration at the tip of a notch. As the U_{pot} is much higher than U_{surf} , the fracture is unstable.



(a)



(b)

Figure 18: (a) Stress vs. strain plot, and (b) complete fracture of a thin polySi film having $l = 23 \mu\text{m}$ at the macroscopic level

Secondly, the length of the model is further increased to $l = 23.0 \mu\text{m}$ to have a more realistic model domain and discretized with a much larger finite elements discretization without changing any other parameters, such that the size of the elements is approximately equal to the size of RVE in Section 3.3.1. It is purposefully avoided to have a refined mesh in the central region to have a more general simulation results without any influence of the mesh density. The stress vs. strain plot and fracture are shown in Figure 18. The stress concentration at the tip of the defect is reduced due to an increase in the length of a model, thus resulting in a slightly higher value of the fracture stress

in Figure 18a as compared with Figure 17a.

5 Experimental observations

The microstructure and the roughness of a thin polySi film have been experimentally analyzed, in the context of this research, to have a consistent comparison between the experiment and simulation results. For these experiments, a 240 nm thick polySi layer has been deposited on top of an oxidized Si substrate. In order to extract the Young's modulus as well as the fracture strain of the deposited polySi layer, on-chip tensile test structures have been manufactured. The principle and process of the preparation of samples are elaborated in [27–32]. Automated crystallographic orientation mapping

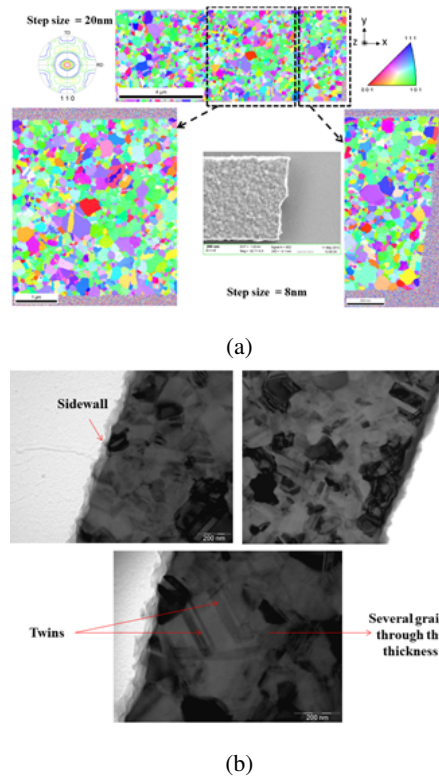
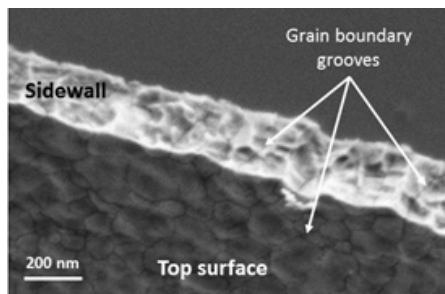


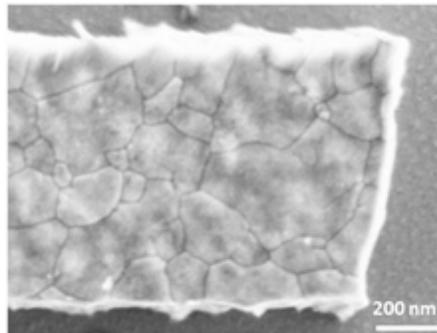
Figure 19: (a) Top view of the out-of-plane orientation map of a 240 nm-thick and 4 μm -wide polySi sample. Orientation maps of 20 and 8 nm as step size and 111 pole figure, (b) Bright field TEM images of the polySi sample

in a transmission electron microscope (ACOM-TEM) is a newly developed technique attached to TEM, which is used in the present work to determine the local orientation of polySi grains. The electron diffraction (ED) patterns, instead of Kikuchi patterns, are collected with an external charge coupled digital (CCD) camera. The acquired ED pattern is then stored in a computer and compared (off-line) with the pre-calculated templates and the best match is selected [33]. The experimental measurements were performed by Philips CM20 operating at 200 kV and equipped with a LaB6 gun and an external source device, DigiSTAR® developed by NanoNEGAS for ACOM-TEM

experiments [33]. Figure 19a shows ACOM-TEM orientation mapping recorded by a 20 nm step size and an acquisition frequency of around 100 frames per second for all the sample surface analysis. In order to increase the quality of the orientation map and to highlight the microstructure of the sample, the step size was decreased to 8 nm and 60 frames per second. The average grain size is estimated to be ≈ 110 nm with a standard deviation of 90 nm. The large standard deviation is due to the log-normal distribution of the grain size. The microstructure is composed of a large number of small grains with a size smaller than 100 nm and also few larger grains characterised by a diameter larger than 500 nm (as seen in Figure 19a). The sample exhibits a preferential (110) out-of-plane fiber texture and no specific in-plane orientation is emerged. As mentioned above, the ACOM-TEM analysis of the polySi film reveals a complex microstructure with the presence of numerous twinned grains. By increasing the resolution (decreasing the step size to 8 nm), the twins are clearly visible, as confirmed by TEM images in Figure 19b. The scanning electron microscope (SEM) observation



(a)



(b)

Figure 20: (a) SEM image of the sidewall of the 240 nm-thick polySi sample, (b) SEM image of the top view of fracture zone for 900 nm-wide polySi sample

of the sidewall shows the presence of one or two grains through the thickness (Figure 20a) as used in the simulated geometry (Section 3.2). Concerning the fracture process, the crack path appears to be clearly transgranular, as shown in Figure 20b. The fracture strain extracted from this test structure is 0.96% ($\pm 0.07\%$). It corresponds to a fracture stress of about 1.41 GPa (± 0.1) for Young's modulus of 147 GPa [27].

The fracture of a brittle polySi film is initiated from critical flaws located on the external surfaces, i.e., the sidewalls, top and bottom surfaces [34] as modelled in the last section. These flaws are generated by the micromachining processes during the

sample preparation. They might be micro structural defects as grain boundary grooves that emerge on external surfaces and/or geometrical imperfections directly generated by the preparation process, as shown in Figure 20a. The nature and location of the critical flaws depend on the preparation process and the sample thickness, as their microstructure is governed by both. The fracture is initiated at the flaw corresponding to the highest stress concentration which is governed by several factors, such as the morphology, density, size of the flaw, local microstructure orientation, local fracture toughness, and the local residual stress state. In this specific case, the sidewall roughness appears larger than that of the top and bottom surfaces. Thus, the critical flaws are most probably located on the sidewalls. Nevertheless, although the grain boundary grooves emerge on the sidewalls and are visible, it is not possible to precisely conclude that they constitute the critical flaws for the initiation of the fracture. More in-depth studies of the effect of sidewall roughness on the fracture behaviour of a thin polySi film have to be performed to identify and characterize the population of the main critical flaws. These results could be used to prepare a more accurate model for the simulations.

6 Conclusions

The fracture of a thin polySi film has been simulated by the DG/ECL framework with a specific focus on the influence of an out-of-plane grain orientation on the fracture process. This is achieved by the 2-scale approach, where the influence of the grain orientation on the fracture at the mesoscopic length RVE is linked with the fracture of a thin polySi film at the MEMS length scale through an average ECL. The interface (cohesive) elements are inserted in-between the bulk elements from the beginning of the simulation itself. As the ECL is activated only at the node where the effective stress reaches the fracture strength, no *a priori* knowledge of crack path as well as the remeshing of the geometry are required. This advantage of the suggested framework allows the parallelization of the code. A novel model to compute the effective fracture strength σ_c of anisotropic material is proposed, which also satisfies the symmetry requirement of the unit cube of polySi. The results obtained by the numerical simulations are broadly in accordance with the experimentally observed fact that irrespective of the orientation of crystals, crack eventually occurs and propagates along an approximately (1 1 1) cleavage plane, as the surface energy of this orientation plane is smaller than the (1 0 0) and (1 1 0) planes. The simulation of a thin polySi film at the mesoscopic level results in the fracture stress and strain of $\approx 1.0 \times 10^{-3}$ TPa and 0.6%, respectively, and $G_c \approx 3.0 \times 10^{-6}$ N/ μ m. All these values are in-between the values corresponding to the out-of-plane grain orientations (1 1 0) and (1 1 1). This means that, the fracture is always propagated along the weakest cohesive element with an out-of-plane orientation close to the orientation of (1 1 0) or (1 1 1) planes. The simulation of a thin polySi film at the macroscopic level demonstrates that the average macroscopic cohesive law can be accurately extracted at the end of the stable fracture with a much larger size of the elements (\approx size of the RVE), thus considerably reducing the computational time. Both the simulation results (meso- and macroscopic level) are found to be closely matching with the several experimental results available in the open literature.

The fracture of a polySi thin film is experimentally performed in-house by the on-chip fracture test, with (1 1 0) average local preferential orientation of the sample in the out-of-plane direction. The in-plane orientations are random, but based on the symmetry-equivalent cleavage planes, (1 0 0) and (1 1 0) orientations influence the

fracture behaviour of this particular sample of polySi. The values of fracture strain and stress are found to be 0.96% ($\pm 0.07\%$) and 1.41 GPa (± 0.1) with this setup. Thus, the fracture stress, as predicted, is in-between the fracture strengths along the (1 0 0) and (1 1 0) cleavage planes. The comparison between the simulations and in-house experiments show that the fracture stress obtained by the simulations is close to, but slightly lower than, the experiments. This could be due to the fact that the σ_c in the simulations is computed by the weighted average values of fracture strength along the (1 0 0), (1 1 0), and (1 1 1) in-plane orientations, where as the sample used in the experiment has random in-plane orientations with higher influence of the (1 0 0) and (1 1 0) orientations. The crack path of the fracture is found to be transgranular by both the experiments and simulations. The present work can be extended in the future by studying and incorporating the influence of the side wall roughness and other flaws on the fracture behaviour of a thin polySi film.

7 Acknowledgements

The authors gratefully acknowledge the financial support from F. R. S. - F. N. R. S. under the project number FRFC 2.4508.11.

References

- [1] Frank W. DelRio, Martin L. Dunn, Brad L. Boyce, Alex D. Corwin, and Maarten P. De Boer. The effect of nanoparticles on rough surface adhesion. *Journal of Applied Physics*, 99(10):104304, 2006.
- [2] Wan Suwito, Martin L. Dunn, Shawn J. Cunningham, and David T. Read. Elastic moduli, strength, and fracture initiation at sharp notches in etched single crystal silicon microstructures. *Journal of Applied Physics*, 85(7):3519–3534, 1999.
- [3] Jr. Sharpe, W.N., K.T. Turner, and R.L. Edwards. Tensile testing of polysilicon. *Experimental Mechanics*, 39(3):162–170, 1999.
- [4] W.N. Sharpe, Kamili M. Jackson, K.J. Hemker, and Z. Xie. Effect of specimen size on young's modulus and fracture strength of polysilicon. *Microelectromechanical Systems, Journal of*, 10(3):317–326, 2001.
- [5] Staffan Greek, Fredric Ericson, Stefan Johansson, Matthias FÄ¼rtsch, and Arnold Rump. Mechanical characterization of thick polysilicon films: Young's modulus and fracture strength evaluated with microstructures. *Journal of Micromechanics and Microengineering*, 9(3):245, 1999.
- [6] W. N. Sharpe, B. Yuan, R. Vaidyanathan, and R. L. Edwards. New test structures and techniques for measurement of mechanical properties of mems materials. In *Microlithography and Metrology in Micromachining II*, volume 2880 of *Society of Photo-Optical Instrumentation Engineers (SPIE) Conference Series*, pages 78–91, 1996.
- [7] W.W. Van Arsdell and S.B. Brown. Subcritical crack growth in silicon mems. *Microelectromechanical Systems, Journal of*, 8(3):319–327, 1999.

- [8] L. Noels and R. Radovitzky. A general discontinuous Galerkin method for finite hyperelasticity. formulation and numerical applications. *International Journal for Numerical Methods in Engineering*, 68(1):64–97, 2006.
- [9] L. Noels and R. Radovitzky. A new discontinuous Galerkin method for Kirchhoff-Love shells. *Computer Methods in Applied Mechanics and Engineering*, 197(33-40):2901 – 2929, 2008.
- [10] G. Becker, C. Geuzaine, and L. Noels. A one field full discontinuous Galerkin method for Kirchhoff-Love shells applied to fracture mechanics. *Computer Methods in Applied Mechanics and Engineering*, 200(45-46):3223 – 3241, 2011.
- [11] G. Becker and L. Noels. A full-discontinuous Galerkin formulation of nonlinear Kirchhoff-Love shells: elasto-plastic finite deformations, parallel computation, and fracture applications. *International Journal for Numerical Methods in Engineering*, 93(1):80–117, 2013.
- [12] D. S. Dugdale. Yielding of steel sheets containing slits. *Journal of the Mechanics and Physics of Solids*, 8(2):100–104, 1960.
- [13] G. I. Barenblatt. The mathematical theory of equilibrium cracks in brittle fracture. volume 7, pages 55–129. Elsevier, 1962.
- [14] A. Hillerborg, M. Modéer, and P.-E. Petersson. Analysis of crack formation and crack growth in concrete by means of fracture mechanics and finite elements. *Cement and Concrete Research*, 6(6):773 – 781, 1976.
- [15] G. T. Camacho and M. Ortiz. Computational modelling of impact damage in brittle materials. *International Journal of Solids and Structures*, 33(20-22):2899–2938, 1996.
- [16] M. Ortiz and A. Pandolfi. Finite-deformation irreversible cohesive elements for three-dimensional crack propagation analysis. *International Journal for Numerical Methods in Engineering*, 44(9):1267–1282, 1999.
- [17] J. Mergheim, E. Kuhl, and P. Steinmann. A hybrid discontinuous Galerkin/interface method for the computational modelling of failure. *Communications in Numerical Methods in Engineering*, 20(7):511–519, 2004.
- [18] Clemens V. Verhoosel, Joris J. C. Remmers, Miguel A. Gutiérrez, and René de Borst. Computational homogenization for adhesive and cohesive failure in quasi-brittle solids. *International Journal for Numerical Methods in Engineering*, 83(8-9):1155–1179, 2010.
- [19] L. Wu, D. Tjahjanto, G. Becker, A. Makradi, A. Jèrusalem, and L. Noels. A micro-meso-model of intra-laminar fracture in fiber-reinforced composites based on a discontinuous Galerkin/cohesive zone method. *Engineering Fracture Mechanics*, 104(0):162–183, 2013.
- [20] Taechung Yi, Lu Li, and Chang-Jin Kim. Microscale material testing of single crystalline silicon: process effects on surface morphology and tensile strength. *Sensors and Actuators A: Physical*, 83(1-3):172–178, 2000.

- [21] Kazuo Sato, Tetsuo Yoshioka, Taeko Ando, Mitsuhiro Shikida, and Tatsuo Kawabata. Tensile testing of silicon film having different crystallographic orientations carried out on a silicon chip. *Sensors and Actuators A: Physical*, 70(1-2):148–152, 1998.
- [22] J. J. Gilman. Direct measurements of the surface energies of crystals. *Journal of Applied Physics*, 31(12):2208–2218, 1960.
- [23] C. Messmer and J. C. Bilello. The surface energy of Si, GaAs, and GaP. *Journal of Applied Physics*, 52(7):4623–4629, 1981.
- [24] M.A. Hopcroft, W.D. Nix, and T.W. Kenny. What is the young’s modulus of silicon? *Microelectromechanical Systems, Journal of*, 19(2):229–238, 2010.
- [25] K. Alzabdeh and M. Ostoja-Starzewski. Micromechanically based stochastic finite elements: length scales and anisotropy. *Probabilistic Engineering Mechanics*, 11(4):205–214, 1996.
- [26] M. Ostoja-Starzewski. Random field models of heterogeneous materials. *International Journal of Solids and Structures*, 35(19):2429–2455, 1998.
- [27] S. Gravier, M. Coulombier, A. Safi, N. Andre, A. Boe, J. P Raskin, and Thomas Pardoën. New on-chip nanomechanical testing laboratory - applications to aluminum and polysilicon thin films. *Microelectromechanical Systems, Journal of*, 18(3):555–569, 2009.
- [28] E. Escobedo-Cousin, S. H. Olsen, T. Pardoën, U. Bhaskar, and J.-P. Raskin. Experimental observations of surface roughness in uniaxially loaded strained si microelectromechanical systems-based structures. *Applied Physics Letters*, 99(24):241906, 2011.
- [29] Umesh Bhaskar, Vikram Passi, Samer Hourri, Enrique Escobedo-Cousin, Sarah H. Olsen, Thomas Pardoën, and Jean-Pierre Raskin. On-chip tensile testing of nanoscale silicon free-standing beams. *Journal of Materials Research*, 27(03):571–579, 2012.
- [30] Vikram Passi, Umesh Bhaskar, Thomas Pardoën, U. Sodervall, Bengt Nilsson, G. Petersson, Mats Hagberg, and J. P Raskin. High-throughput on-chip large deformation of silicon nanoribbons and nanowires. *Microelectromechanical Systems, Journal of*, 21(4):822–829, 2012.
- [31] Ferran Ureña, Sarah H. Olsen, Lidija Šiller, Umesh Bhaskar, Thomas Pardoën, and Jean-Pierre Raskin. Strain in silicon nanowire beams. *Journal of Applied Physics*, 112(11):114506, 2012.
- [32] Umesh Kumar Bhaskar, Thomas Pardoën, Vikram Passi, and Jean-Pierre Raskin. Piezoresistance of nano-scale silicon up to 2 GPa in tension. *Applied Physics Letters*, 102(3):031911–031911–4, 2013.
- [33] M. Galceran, A. Albou, K. Renard, M. Coulombier, P.J. Jacques, and S. Godet. Automatic crystallographic characterization in a transmission electron microscope: Applications to twinning induced plasticity steels and al thin films. *Microscopy and Microanalysis*, 19(03):693–697, 2013.

- [34] T. Tsuchiya, O. Tabata, Jiro Sakata, and Yasunori Taga. Specimen size effect on tensile strength of surface micromachined polycrystalline silicon thin films. In *Micro Electro Mechanical Systems, 1997. MEMS '97, Proceedings, IEEE., Tenth Annual International Workshop on*, pages 529–534, 1997.